
EarthArXiv Cover Page

This is a non-peer-reviewed preprint submission to EarthArXiv. The manuscript is currently under consideration at Nature Geoscience (submitted 02/07/2021). Subsequent versions of this manuscript will likely differ. If accepted, the final version of this manuscript will be available via the 'Peer-reviewed Publication DOI' link.

Magma pressurisation sustains eruptive episode at dome-building Soufrière Hills Volcano

J. Hickey^{1*}, K. Pascal^{2,3}, M. Head¹, J. Gottsmann⁴, N. Fournier⁵, S. Hreinsdottir⁵, R. Syers²

¹ Camborne School of Mines, University of Exeter, United Kingdom

² Montserrat Volcano Observatory, University of the West Indies, Montserrat

³ Seismic Research Centre, University of the West Indies, Trinidad and Tobago

⁴ School of Earth Science, University of Bristol, United Kingdom

⁵ GNS Science, New Zealand

* Corresponding author: James Hickey (j.hickey@exeter.ac.uk)

Emails: j.hickey@exeter.ac.uk, karen_pascal@yahoo.com, m.head2@exeter.ac.uk, j.gottsmann@bristol.ac.uk, N.Fournier@gns.cri.nz, s.hreinsdottir@gns.cri.nz.

1 **Magma pressurisation sustains eruptive episode at dome-building Soufrière Hills Volcano**

2

3 J. Hickey^{1*}, K. Pascal^{2,3}, M. Head¹, J. Gottsmann⁴, N. Fournier⁵, S. Hreinsdottir⁵, R. Syers²

4

5 ¹ Camborne School of Mines, University of Exeter, United Kingdom

6 ² Montserrat Volcano Observatory, University of the West Indies, Montserrat

7 ³ Seismic Research Centre, University of the West Indies, Trinidad and Tobago

8 ⁴ School of Earth Science, University of Bristol, United Kingdom

9 ⁵ GNS Science, New Zealand

10

11 * Corresponding author: James Hickey (j.hickey@exeter.ac.uk)

12

13 **Abstract**

14

15 Dome-building volcanoes are particularly challenging for volcanic hazard assessment, where long-
16 term eruptive episodes can be interspersed with periods of intra-eruptive repose. Defining the end of
17 eruptive episodes is vitally important for the socio-economic recovery of affected communities, but
18 highly problematic due to the potential for prolonged, seemingly low-risk, repose to rapidly transition
19 to dangerous effusive or explosive activity. It is currently unclear what constitutes the end of repose
20 and an eruptive episode. Here we show that analysis of surface deformation can characterise repose
21 and help define an eruptive episode. At Soufrière Hills volcano (SHV) the observed long-term
22 deformation requires the pressure in the magma system to increase with time; time-dependent stress
23 relaxation or crustal creep cannot explain the deformation trends alone. Continued pressurisation
24 within the magmatic system during repose could initiate a renewed eruption, qualifying as sustained
25 unrest and therefore continuation of the eruptive episode. For SHV, persistent magma pressurisation
26 highlights the need for sustained vigilance in the monitoring and management of the volcano and its
27 surroundings, despite the last eruptive activity ending in 2010.

28

29

30 Dome-building volcanoes typically evolve through a process of lava dome formation, with three main
31 activity states identified: inter-eruptive repose (dormant); active with magma being erupted (eruption);
32 and intra-eruptive repose (post-eruption unrest during eruptive episode)¹. Eruption is mostly through
33 effusive dome extrusion, but sudden transitions to explosive behaviour are possible¹⁻⁴. A period of
34 intra-eruptive repose classifies an eruptive episode as continuing, an effect born of the repetitive and
35 cyclic process of dome extrusion and destruction^{1-3,5-7}. However, distinguishing intra-eruptive repose
36 from inter-eruptive repose, through the presence or absence, respectively, of concerning geophysical
37 or geochemical monitoring signals, is difficult¹, and complicates how the end of an eruptive episode is
38 determined. Consequently, the socio-economic recovery of affected communities can be severely
39 impaired, and dome-building volcanoes are particularly challenging for hazard and risk assessment.

40

41 Volcano surface deformation is a common sign of volcanic unrest^{8,9}; deciphering its cause is

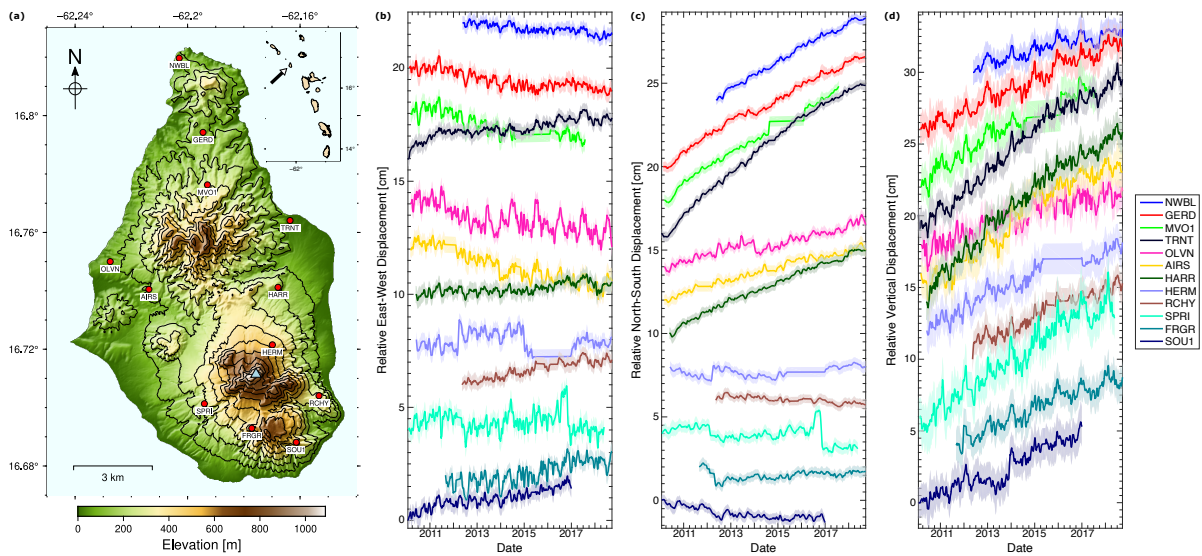
42 fundamental for monitoring and hazard mitigation^{10,11}. Magma supply¹²⁻¹⁸, cooling and contraction¹⁹⁻

43 ²¹, and crystallisation with volatile exsolution²² have been proposed as the main magmatic drivers,
44 but, tectonic^{19,20,23}, hydrothermal^{24–26} and rheological^{16,27–29} processes can also sustain volcano
45 deformation. The variety of different mechanisms present contrasting interpretations of magma
46 system evolution and the development of unrest episodes^{30,31}. Deformation related to viscoelastic
47 rheological processes might indicate a constant or reducing pressure in the magmatic system³⁰, a
48 decrease in eruption potential, and at dome-building volcanoes relate to inter-eruptive repose.
49 Conversely, deformation from magma supply might indicate increased eruption potential with cause
50 for concern, signifying intra-eruptive repose. Uncertainty in the cause of deformation, and
51 characterising periods of repose, is problematic and complicates eruption forecasting, hazard
52 assessment, and risk mitigation^{31,32}.

53

54 Soufrière Hills Volcano (SHV) is an andesitic dome-building volcano on the island of Montserrat
55 (Figure 1), and began its current eruptive episode in 1995. Eruptive activity has been intermittent^{33,34}
56 with periods of intra-eruptive repose generally lasting 1-2 years (Supplementary Figure 1). However,
57 the most recent eruption ended in February 2010 making the current repose period the longest yet
58 recorded. SO₂ observations at SHV since 2010 show steady emissions at an average rate of 374
59 t/day, and fumaroles on the lava dome maintain temperatures up to 610°C³⁵. Swarms of volcano-
60 tectonic (VT) earthquakes have also been recorded, and can correlate with short-term increases in
61 the SO₂ flux³⁵. Continuous GPS (cGPS) measurements show island-wide inflation from 2010 onwards
62 (Figure 1). Globally, 94% of dome-building eruptive episodes last less than 20 years⁵. The current 11-
63 year cessation of surface activity and low level of seismicity, following 15 years of intermittent activity,
64 raise the question of whether the current repose is temporary or, instead, indicative of the end of the
65 eruptive episode. The ambiguity is exacerbated by the presence of surface deformation whose driving
66 processes remain unclear. The longevity of the current repose, and suggestions based on
67 geochemical data that magma supply to SHV potentially ceased in mid-2003³⁶, may indicate that non-
68 magmatic processes (e.g., viscoelastic crustal behaviour²⁷) are now driving the continued
69 deformation. To assess the behaviour and evolution of the SHV magmatic system since 2010, the
70 nature of the current repose, and the relation to ongoing hazard assessment, we analyse the temporal
71 deformation trends using geodetic numerical models and test the hypothesis that viscoelastic crustal
72 behaviour is driving long-term surface inflation.

73



74

75 **Figure 1:** The cGPS network and recorded deformation on Montserrat. (a) DEM of Montserrat
 76 showing cGPS stations with red circles, and the active vent identified with the blue triangle. Inset map
 77 shows the Eastern Caribbean with the island of Montserrat indicated by the arrow. (b) Relative east-
 78 west horizontal deformation with time for the 12 cGPS stations shown in A. Time series are offset in
 79 the y-axis for added clarity. (c) Relative north-south horizontal deformation with time for the 12 cGPS
 80 stations shown in A. Time series are offset in the y-axis for added clarity. (d) Relative vertical
 81 deformation with time for the 12 cGPS stations shown in A. Time series are offset in the y-axis for
 82 added clarity. Shaded bars in B-D indicate 95% confidence bounds.

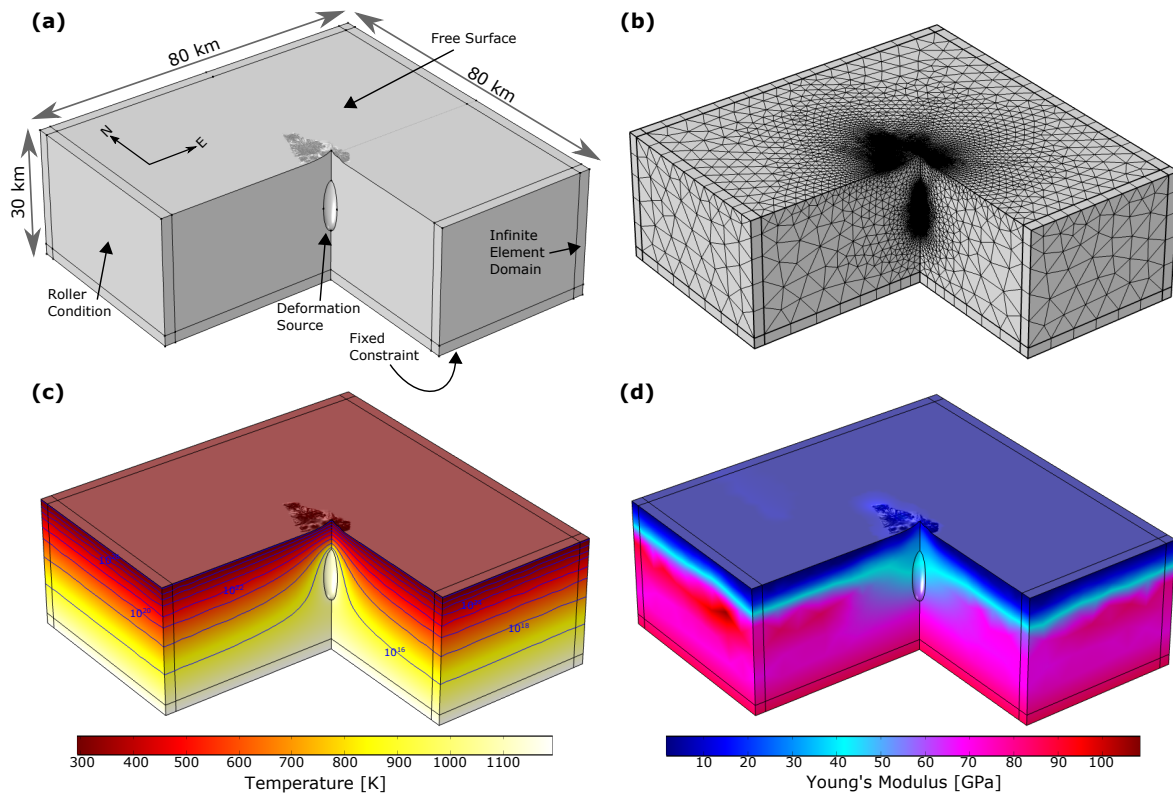
83

84 Deformation Modelling

85

86 The geodetic models used in this study incorporate a temperature-dependent viscoelastic crustal
 87 rheology, topography derived from a Digital Elevation Model (DEM)³⁷ and three-dimensional
 88 variations in mechanical properties derived from seismic tomography³⁸ (Figure 2). Our model outputs
 89 are compared to the 2010-2018 three-dimensional deformation recorded at 12 cGPS sites across
 90 Montserrat, ensuring the widest possible data-model evaluation (Figure 1 & Supplementary Figure 2).
 91 The models are driven using one of four possible time-dependent source functions, to simulate first-
 92 order differences in the temporal evolution of the magmatic system (Figure 3), with stress-based
 93 overpressure (ΔP) and strain-based volume change (ΔV) boundary conditions both being compared.
 94 In all model scenarios, viscoelastic crustal rheology can produce creep and/or recovery behaviour³⁰.

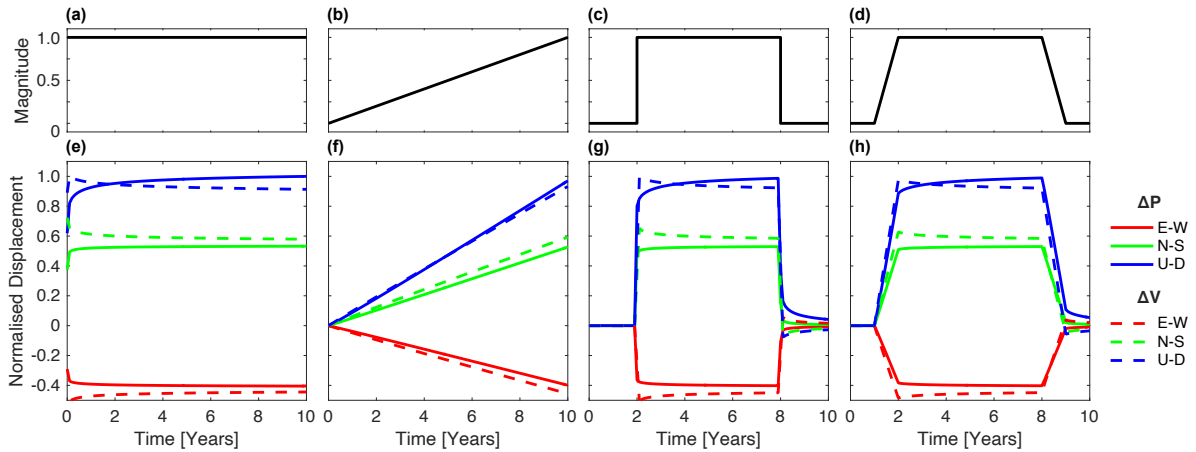
95



96

97 **Figure 2:** *Finite Element Analysis model. (a) Geometry and boundary conditions. A cavity is used to*
 98 *represent the deformation source using a pressure or volume boundary condition and a bordering*
 99 *infinite element domain prevents boundary effects. Roller conditions are assigned to all lateral*
 100 *boundaries, and a fixed constraint is applied to the base of the model. The top surface is free to*
 101 *deform, and incorporates a 10 m DEM of the island of Montserrat. (b) The geometry is meshed with*
 102 *~690,000 tetrahedral elements, with greater mesh density around the source and surface. (c) The*
 103 *modelled steady-state temperature distribution, with contours on the model geometry showing the*
 104 *viscosity used in the viscoelastic model. (d) The three-dimensional distribution of static Young's*
 105 *Modulus derived from a seismic P-wave model³⁸ (see Methods).*

106



107

108 **Figure 3:** Model source functions and results. (a-d) Temporal functions applied to the deformation
 109 source boundary conditions: static (a), ramp (b), instant pulse (c), and gradual pulse (d). (e-h) Model
 110 results (normalized displacement timeseries) for the AIRS cGPS site for the four temporal functions:
 111 static (e), ramp (f), instant pulse (g), and gradual pulse (h). The solid and dashed lines represent the
 112 ΔP and ΔV boundary conditions, respectively, while the colours differentiate the 3 components of
 113 deformation (red: east-west, green: north-south, blue: vertical). Results are normalized to the
 114 maximum absolute deformation across the 3 components and across the 4 model functions (in this
 115 case vertical and static). The model results show different temporal trends in the predicted
 116 displacements according to the temporal source function used. The same temporal trends are seen in
 117 the other cGPS site locations (Supplementary Figures 3 & 4).

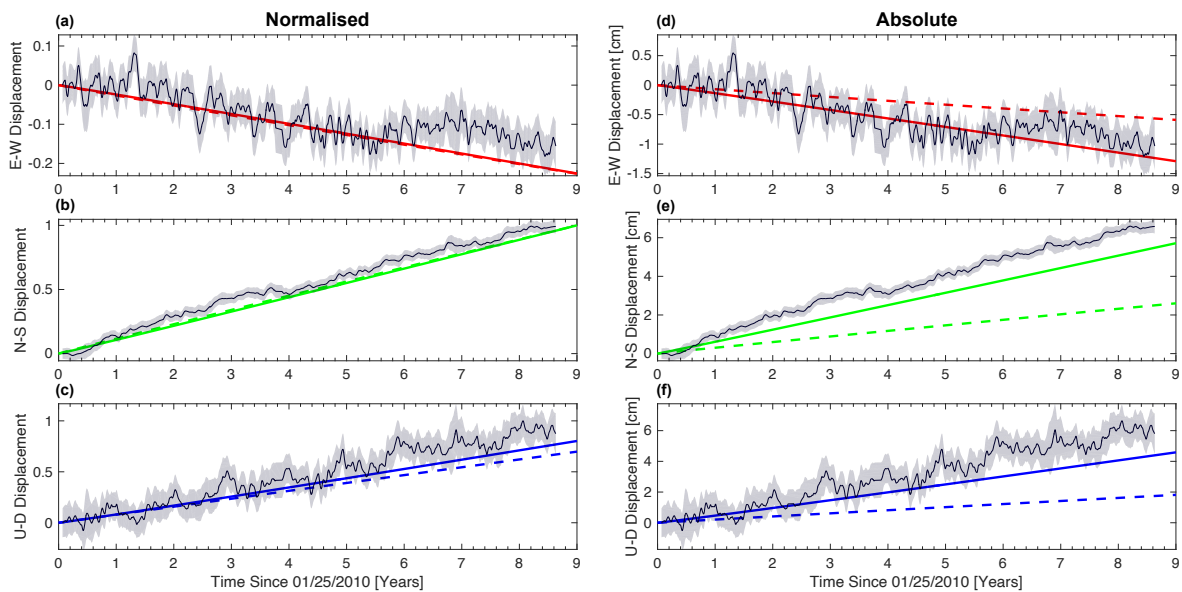
118

119 The four time-dependent source functions produce very different modelled surface displacement
 120 timeseries (Figure 3). However, when compared together, clear deformation patterns emerge which
 121 reflect the (modelled) state of the magma reservoir, with the same temporal patterns reproduced in all
 122 three components of the simulated cGPS data. When the magma reservoir is in a constant state
 123 (Figure 3e), with no pressure or volume increase, we observe minor amounts of viscoelastic creep
 124 (producing inflation) for the ΔP models and minor amounts of viscoelastic relaxation (resulting in
 125 subsidence) for the ΔV models. In both cases the time-dependent viscoelastic surface deformation
 126 becomes insignificant after ~ 4 years with a constant magma reservoir state. In contrast, to produce
 127 substantial magnitudes of continuous deformation with time, and/or continued deformation over
 128 timescales greater than 4 years, requires the reservoir pressure or volume to be increasing (Figures
 129 3f & 3h).

130

131 Model results obtained with the ramp source function (Figure 3f) provide our best-fit to the observed
 132 temporal deformation trends (Figure 4). The recorded deformation data time-series show increasing
 133 deformation (vertical uplift and radial spreading) at a near-constant rate between early-2010 and late-
 134 2018 (Figure 1). An increasing amount of deformation over this timescale at a near-constant rate is
 135 only achievable using the ramped time-dependent source function, and the comparison between the
 136 normalised modelled and observed displacements shows a very close match in the temporal patterns
 137 (Figure 4a-c & Supplementary Figure 5). Comparisons between the absolute modelled and observed
 138 temporal displacements also show a close match (Figure 4d-f c & Supplementary Figure 6), and could
 139 possibly be improved further by focussing on the spatial patterns of displacement to optimise a
 140 pressure or volume change. However, this was beyond the scope of the current study.

141



142

143 **Figure 4:** Normalised and absolute model-data comparison for cGPS site GERD and the ramp
 144 temporal source function. (a-c) Normalised surface displacements for the east-west (a), north-south
 145 (b) and vertical (c) components, where the thin black line and shaded grey region display the
 146 recorded deformation and error bounds, and the solid and dashed coloured lines show the model
 147 results for a ΔP and ΔV boundary condition, respectively. Model and data are normalized to the
 148 maximum absolute deformation across the 3 components (in this case vertical). (d-f) Same as a-c but
 149 the model and data have not been normalized.

150

151 Magma System Pressurisation

152

153 Our results indicate that viscoelastic crustal deformation alone cannot explain the amplitude or
154 temporal pattern of ongoing long-term surface deformation observed at SHV since early 2010.
155 Modelled surface displacements (Figure 3) highlight that continued deformation over the timescales
156 recorded in the cGPS data are only achievable when the magma reservoir is subject to an increasing
157 pressure or volume. In our analysis we compared both ΔP and ΔV source boundary conditions, with
158 the effects of viscoelasticity producing increasing uplift (via creep) in the ΔP models, and post-uplift
159 subsidence (via relaxation) in the ΔV models³⁰. For the thermomechanical conditions inferred beneath
160 SHV, the choice of ΔP or ΔV becomes arbitrary when using our best-fit source function, the ramp, as
161 their viscous effects (creep or relaxation) are indistinguishable on the timescales observed. Their
162 viscoelastic effects are constantly overprinted by the elastic portion of deformation from the increasing
163 (ramped) pressure or volume change (due to Boltzmann superposition¹²), and hence the absence of
164 prolonged viscous creep or relaxation maintains a near-linear temporal uplift pattern. Consequently,
165 their normalised temporal deformation trends are broadly equal (Figure 4). It is noted, however, that
166 the effects of viscoelasticity are still evident when compared to a purely elastic model, for example
167 producing elevated uplift for the ΔP case^{12,18,30}.

168

169 The increasing magma reservoir pressure or volume at SHV since 2010 could be caused by a variety
170 of mechanisms. The most natural driving force to assume is renewed or continued magma supply
171 from a deep source region, which could initially seem in contrast to a proposed stop in the magma
172 supply in 2003 inferred from geochemical results³⁶. However, magma supply from depth could still be
173 occurring and driving this deformation if the magma supplied between ~2003 and present-day is still
174 being stored within the magmatic system, and has not been erupted. A scenario of continued magma
175 supply implies there was a possible change in the magmatic system around 2003, and SHV has only
176 erupted magma(s) supplied pre-2003 in the 2003-2010 period, which are subsequently recorded in
177 the geochemical results³⁶. Continued magma supply would also be consistent with post-2003 eruptive
178 activity and high temperature fumaroles on the dome³⁵, and could be driven in part by ongoing
179 degassing that maintains a pressure gradient between shallow magma storage and deeper magma
180 production³⁹.

181

182 Alternative mechanisms to explain the inferred increasing pressure or volume relate to the role of
183 volatiles within the magmatic system. Volatile exsolution caused by magma crystallisation (second
184 boiling) can drive volume increases within a magma reservoir^{22,40,41} and cannot be ruled out at SHV.
185 However, it is beyond the scope of this paper to test whether a second boiling process alone can
186 generate a volume change or pressurisation of the required magnitude to explain the observed
187 deformation, especially in an open system that is still emitting significant amounts of SO₂³⁵. The
188 continued gas emissions suggest that large quantities of volatiles are present within the magmatic
189 plumbing system; it is therefore conceivable that a steady supply of volatiles, originating from a
190 deeper source region and decoupled from the melt, is fluxing upwards through the system^{35,42}. If
191 volatile pathways to the surface are fixed, accounting for the steady gas emission rates³⁵, then
192 additional volatiles may accumulate within the subsurface system and drive reservoir volume or
193 pressure increases to promote surface deformation. Even without a decoupled supply of volatiles from
194 depth or a second boiling process, volumetric accumulation of exsolved volatiles may still be driving
195 the recorded deformation through the segregation, reorganisation and/or compaction of a transcrustal
196 magmatic system (TCMS)^{35,43,44}. In this scenario, volatiles could drive deformation without magma
197 supply by buoyantly accumulating while a hot crystal mush is destabilised and reorganised. Several
198 studies, using geochemical, seismic, gravity, deformation and gas emission data, have suggested
199 such a transcrustal magmatic system beneath SHV^{35,45–47}.

200

201 **Sustaining an eruptive episode**

202

203 The different magmatic processes that have been suggested as possible causes for the observed
204 long-term surface deformation at SHV have mechanisms that promote increases in pressure and/or
205 volume within a reservoir. Our models considered both pressure and volume boundary conditions, but
206 we cannot distinguish between the two for our best-fit source function owing to the similar temporal
207 deformation trends they produce (Figures 3 and 4). Continued geophysical observations and
208 additional (e.g., gravimetric) data might be able to differentiate between the suggested driving
209 mechanisms and the pressure or volume boundary condition in the future. It is also possible that two
210 or more of our suggested mechanisms are occurring simultaneously, with or without viscoelastic

211 deformation. Regardless, it is clear from our results that viscoelastic crustal deformation alone cannot
212 explain the ongoing deformation, and some component of magma system pressurisation (where the
213 term pressurisation is also inclusive of volume expansion) is required. Moreover, the strong likelihood
214 of significant volatiles in the SHV magmatic system would imply a compressible magma able to
215 accommodate a certain amount of mass addition without producing a pressurisation driving surface
216 deformation^{41,48}. Therefore, the presence of measured surface deformation given a compressible
217 magma further reinforces the need for an active magma pressurisation over a passive viscoelastic
218 deformation mechanism.

219

220 Continued magma system pressurisation at SHV implies ongoing volcanic unrest⁸, and therefore the
221 current repose should be classified as intra-eruptive. Despite its pressurising magmatic system, the
222 volcano has remained in a state of protracted intra-eruptive repose, in contrast to the preceding short
223 intra-eruptive repose periods. The extended length of the current repose represents a possible major
224 change to the behaviour of the sub-volcanic system compared to its pre-2010 behaviour, and may
225 imply that the deformation and unrest observed during the previous intra-eruptive periods was driven
226 by a different mechanism to that (or those) driving the current long-term deformation (2010 onwards).
227 A change in the mechanism driving the deformation draws parallels to suggestions of a stop in the
228 magma supply in 2003³⁶, but would imply a different time for any changes, and we also do not rule
229 out continued magma supply as a possible cause for the ongoing deformation. More accurately
230 identifying the nature of the mechanism(s) driving the current deformation, alongside further
231 constraints from more geophysics, geochemistry and petrology, will allow for improved longer-term
232 activity forecasting and hazard assessment to be conducted. However, given the solitary role of a
233 viscoelastic rheological crustal response can be ruled out, the continued pressurisation within the
234 magmatic system is inconsistent with inter-eruptive repose and indicates a state of unrest with
235 potential for renewed eruptive activity. Consequently, while the most recent eruptive activity ended in
236 2010, this may not signal the end of the current eruptive episode of the volcano.

237

238 **References**

239

240 1. Sheldrake, T. E., Sparks, R. S. J., Cashman, K. V., Wadge, G. & Aspinall, W. P. Similarities

- 241 and differences in the historical records of lava dome-building volcanoes: Implications for
242 understanding magmatic processes and eruption forecasting. *Earth-Science Rev.* **160**, 240–
243 263 (2016).
- 244 2. Ogburn, S. E., Loughlin, S. C. & Calder, E. S. The association of lava dome growth with major
245 explosive activity ($VEI \geq 4$): DomeHaz, a global dataset. *Bull. Volcanol.* **77**, (2015).
- 246 3. Sparks, R. S. J. Causes and consequences of pressurisation in lava dome eruptions. *Earth*
247 *Planet. Sci. Lett.* **150**, 177–189 (1997).
- 248 4. Newhall, C. G. & Melson, W. G. Explosive activity associated with the growth of volcanic
249 domes. *J. Volcanol. Geotherm. Res.* **17**, 111–131 (1983).
- 250 5. Wolpert, R. L., Ogburn, S. E. & Calder, E. S. The longevity of lava dome eruptions. *J.*
251 *Geophys. Res. Solid Earth* **121**, 676–686 (2016).
- 252 6. Lerner, G. A., Cronin, S. J., Bebbington, M. S. & Platz, T. The characteristics of a multi-
253 episode volcanic regime: the post-AD 960 Maero Eruptive Period of Mt. Taranaki (New
254 Zealand). *Bull. Volcanol.* **81**, (2019).
- 255 7. Odbert, H. M., Stewart, R. C. & Wadge, G. Cyclic phenomena at the Soufrière Hills Volcano,
256 Montserrat. *Geol. Soc. London, Mem.* **39**, 41–60 (2014).
- 257 8. Phillipson, G., Sobradelo, R. & Gottsmann, J. Global volcanic unrest in the 21st century: An
258 analysis of the first decade. *J. Volcanol. Geotherm. Res.* **264**, 183–196 (2013).
- 259 9. Sparks, R. S. J., Biggs, J. & Neuberg, J. W. Monitoring Volcanoes. *Science (80-)*. **335**, 1310–
260 1311 (2012).
- 261 10. Biggs, J. & Pritchard, M. E. Global volcano monitoring: What does it mean when volcanoes
262 deform? *Elements* **13**, 17–22 (2017).
- 263 11. Dzurisin, D. A comprehensive approach to monitoring volcano deformation as a window on the
264 eruption cycle. *Rev. Geophys.* **41**, 1–29 (2003).
- 265 12. Hickey, J., Gottsmann, J., Nakamichi, H. & Iguchi, M. Thermomechanical controls on magma
266 supply and volcanic deformation: application to Aira caldera, Japan. *Sci. Rep.* **6**, 32691 (2016).
- 267 13. Odbert, H. M. *et al.* Volcano geodesy at the Soufriere Hills Volcano, Montserrat: a review.
268 *Geol. Soc. London, Mem.* **39**, 195–217 (2014).
- 269 14. Delgado, F., Pritchard, M., Samsonov, S. & Córdova, L. Renewed Post-eruptive Uplift
270 Following the 2011–2012 Rhyolitic Eruption of Cordón Caulle (Southern Andes, Chile):

- 271 Evidence for Transient Episodes of Magma Reservoir Recharge During 2012–2018. *J.*
272 *Geophys. Res. Solid Earth* **123**, 9407–9429 (2018).
- 273 15. Le Mevel, H., Gregg, P. M. & Feigl, K. L. Magma injection into a long-lived reservoir to explain
274 geodetically measured uplift: Application to the 2007-2014 unrest episode at Laguna del Maule
275 volcanic field, Chile. *J. Geophys. Res. Solid Earth* **121**, 6092–6108 (2016).
- 276 16. Parks, M. M. *et al.* From quiescence to unrest: 20years of satellite geodetic measurements at
277 Santorini volcano, Greece. *J. Geophys. Res. Solid Earth* **2**, 1–20 (2014).
- 278 17. Galetto, F., Bagnardi, M., Acocella, V. & Hooper, A. Noneruptive Unrest at the Caldera of
279 Alcedo Volcano (Galápagos Islands) Revealed by InSAR Data and Geodetic Modeling. *J.*
280 *Geophys. Res. Solid Earth* **124**, 3365–3381 (2019).
- 281 18. Gottsmann, J. & Odbert, H. The effects of thermomechanical heterogeneities in island arc
282 crust on time-dependent preeruptive stresses and the failure of an andesitic reservoir. *J.*
283 *Geophys. Res. Solid Earth* **119**, 4626–4639 (2014).
- 284 19. Parker, A. L., Biggs, J. & Lu, Z. Investigating long-term subsidence at Medicine Lake Volcano,
285 CA, using multitemporal InSAR. *Geophys. J. Int.* **199**, 844–859 (2014).
- 286 20. Parker, A. L., Biggs, J. & Lu, Z. Time-scale and mechanism of subsidence at Lassen Volcanic
287 Center, CA, from InSAR. *J. Volcanol. Geotherm. Res.* **320**, 117–127 (2016).
- 288 21. Hamling, I. J., Hreinsdóttir, S. & Fournier, N. The ups and downs of the TVZ: Geodetic
289 observations of deformation around the Taupo Volcanic zone, New Zealand. *J. Geophys. Res.*
290 *Solid Earth* **120**, 4667–4679 (2015).
- 291 22. Caricchi, L., Biggs, J., Annen, C. & Ebmeier, S. The influence of cooling, crystallisation and re-
292 melting on the interpretation of geodetic signals in volcanic systems. *Earth Planet. Sci. Lett.*
293 **388**, 166–174 (2014).
- 294 23. Bonforte, A., Fanizza, G., Greco, F., Matera, A. & Sulpizio, R. Long-term dynamics across a
295 volcanic rift: 21 years of microgravity and GPS observations on the southern flank of Mt. Etna
296 volcano. *J. Volcanol. Geotherm. Res.* **344**, 174–184 (2017).
- 297 24. Fournier, N. & Chardot, L. Understanding volcano hydrothermal unrest from geodetic
298 observations: Insights from numerical modeling and application to White Island volcano, New
299 Zealand. *J. Geophys. Res. Solid Earth* **117**, 1–16 (2012).
- 300 25. Rouwet, D. *et al.* Recognizing and tracking volcanic hazards related to non-magmatic unrest: a

- 301 review. *J. Appl. Volcanol.* **3**, 17 (2014).
- 302 26. González, P. J., Singh, K. D. & Tiampo, K. F. Shallow Hydrothermal Pressurization before the
303 2010 Eruption of Mount Sinabung Volcano, Indonesia, Observed by use of ALOS Satellite
304 Radar Interferometry. *Pure Appl. Geophys.* **172**, 3229–3245 (2015).
- 305 27. Segall, P. Repressurization following eruption from a magma chamber with a viscoelastic
306 aureole. *J. Geophys. Res. Solid Earth* **121**, 8501–8522 (2016).
- 307 28. Segall, P. Magma chambers: What we can, and cannot, learn from volcano geodesy. *Philos.*
308 *Trans. R. Soc. A Math. Phys. Eng. Sci.* **377**, (2018).
- 309 29. Novoa, C. *et al.* Viscoelastic relaxation: A mechanism to explain the decennial large surface
310 displacements at the Laguna del Maule silicic volcanic complex. *Earth Planet. Sci. Lett.* **521**,
311 46–59 (2019).
- 312 30. Head, M., Hickey, J., Gottsmann, J. & Fournier, N. The Influence of Viscoelastic Crustal
313 Rheologies on Volcanic Ground Deformation: Insights From Models of Pressure and Volume
314 Change. *J. Geophys. Res. Solid Earth* (2019). doi:10.1029/2019jb017832
- 315 31. Pritchard, M. E., Mather, T. A., McNutt, S. R., Delgado, F. J. & Reath, K. Thoughts on the
316 criteria to determine the origin of volcanic unrest as magmatic or non-magmatic. *Philos. Trans.*
317 *R. Soc. A Math. Phys. Eng. Sci.* **377**, (2019).
- 318 32. Poland, M. P. & Anderson, K. R. Partly Cloudy With a Chance of Lava Flows: Forecasting
319 Volcanic Eruptions in the Twenty-First Century. *J. Geophys. Res. Solid Earth* **125**, 1–32
320 (2020).
- 321 33. Sparks, R. S. J. & Young, S. R. The eruption of Soufriere Hills Volcano, Montserrat (1995-
322 1999): overview of scientific results. *Geol. Soc. London, Mem.* **21**, 45–69 (2002).
- 323 34. Wadge, G. *et al.* An overview of the eruption of Soufrière Hills Volcano, Montserrat from 2000
324 to 2010. *Geol. Soc. London, Mem.* **39**, 1–39 (2014).
- 325 35. Christopher, T. E. *et al.* Crustal-scale degassing due to magma system destabilization and
326 magma-gas decoupling at Soufriere Hills Volcano, Montserrat. *Geochemistry Geophys.*
327 *Geosystems* **16**, 2797–2811 (2015).
- 328 36. McGee, L. *et al.* Volatile behaviour in the 1995-2010 eruption of the Soufrière Hills Volcano,
329 Montserrat recorded by U-series disequilibria in mafic enclaves and andesite host. *Earth*
330 *Planet. Sci. Lett.* **524**, 115730 (2019).

- 331 37. Stinton, A. A new Digital Elevation Model of the Soufrière Hills volcano, Montserrat. *Open File*
332 *Rep. OFR 15-01 1*, 1–18 (2015).
- 333 38. Paulatto, M. *et al.* Magma chamber properties from integrated seismic tomography and
334 thermal modeling at Montserrat. *Geochemistry, Geophys. Geosystems* **13**, 1–18 (2012).
- 335 39. Girona, T., Costa, F. & Schubert, G. Degassing during quiescence as a trigger of magma
336 ascent and volcanic eruptions. *Sci. Rep.* **5**, 1–7 (2015).
- 337 40. Yoshimura, S. & Nakamura, M. Carbon dioxide transport in crustal magmatic systems. *Earth*
338 *Planet. Sci. Lett.* **307**, 470–478 (2011).
- 339 41. Caricchi, L., Townsend, M., Rivalta, E. & Namiki, A. The build-up and triggers of volcanic
340 eruptions. *Nat. Rev. Earth Environ.* (2021). doi:10.1038/s43017-021-00174-8
- 341 42. Caricchi, L., Sheldrake, T. E. & Blundy, J. Modulation of magmatic processes by CO₂ flushing.
342 *Earth Planet. Sci. Lett.* **491**, 160–171 (2018).
- 343 43. Sparks, R. S. J. & Cashman, K. V. Dynamic magma systems: Implications for forecasting
344 volcanic activity. *Elements* **13**, 35–40 (2017).
- 345 44. Cashman, K. V., Sparks, R. S. J. & Blundy, J. D. Vertically extensive and unstable magmatic
346 systems: A unified view of igneous processes. *Science (80-.)*. **355**, (2017).
- 347 45. Gottsmann, J., Flynn, M. & Hickey, J. The Transcrustal Magma Reservoir Beneath Soufrière
348 Hills Volcano, Montserrat: Insights From 3-D Geodetic Inversions. *Geophys. Res. Lett.* **47**,
349 (2020).
- 350 46. Paulatto, M. *et al.* Vertically Extensive Magma Reservoir Revealed From Joint Inversion and
351 Quantitative Interpretation of Seismic and Gravity Data. *J. Geophys. Res. Solid Earth* **124**,
352 11170–11191 (2019).
- 353 47. Edmonds, M., Kohn, S. C., Hauri, E. H., Humphreys, M. C. S. & Cassidy, M. Extensive, water-
354 rich magma reservoir beneath southern Montserrat. *Lithos* **252–253**, 216–233 (2016).
- 355 48. McCormick Kilbride, B., Edmonds, M. & Biggs, J. Observing eruptions of gas-rich
356 compressible magmas from space. *Nat. Commun.* **7**, 13744 (2016).

357

358 **Acknowledgements**

359

360 JH acknowledges a travel grant from the Montserrat Volcano Observatory / Seismic Research Centre
361 that stimulated this work. MH is supported by a NERC GW4+ Doctoral Training Partnership
362 studentship from the Natural Environment Research Council [NE/L002434/1] and is thankful for the
363 support and additional funding from CASE partner, GNS Science. JG acknowledges funding from the
364 NERC (NE/E007961/1). We thank Jenni Barclay, Thomas Christopher, Luca Caricchi, Graham Ryan,
365 Lucy McGee and Jane Scarrow for productive discussions on this topic.

366

367 **Author Contributions**

368

369 JH, KP, JG, NF and MH devised the study. JH conducted all the numerical models and analysed the
370 results. KP and SH processed the GPS data, which RS also helped to collect. JH wrote the
371 manuscript with input and discussion from all authors.

372

373 **Competing Interests**

374

375 The authors declare no competing interests.

376

377 **Methods and Materials**

378

379 *GPS data*

380 Geodetic data have been collected continuously at SHV since 1995¹³. The dataset for the 2010-2018
381 time-period consists of the daily timeseries obtained at 12 on-island cGPS sites, using mostly Trimble
382 NetRS and NetR9 receivers, and Trimble Chokering and Zephyr Geoteric 1-2 antennas. The daily
383 GPS data are first converted into RINEX format, before being processed with GAMIT/GLOBK⁴⁹, which
384 uses the double-differencing processing methodology. During the GAMIT step, loosely constrained
385 coordinates for the GPS sites and satellites are calculated in the ITRF14 coordinate system, removing
386 any displacements caused by equipment changes. During the GLOBK step, a set of reference
387 stations distributed globally, with known coordinates, provides external constraints and the stabilized
388 GPS station coordinates are calculated in a Caribbean reference frame¹³ to remove the regional
389 tectonic component from the displacements.

390

391 *Model Setup*

392 We use Finite Element Analysis (FEA) with COMSOL Multiphysics v5.4 to model and analyse the
 393 recorded surface deformation. Our 3D model has surface topography provided by a 10 m resolution
 394 Digital Elevation Model (DEM) of the island of Montserrat³⁷, and boundary conditions include a fixed
 395 constraint on the base of the model, roller conditions on the lateral boundaries and a free surface at
 396 the top of the model^{12,50} (Figure 2). An infinite element domain surrounds the exterior of the model
 397 geometry to prevent boundary effects impacting the results of the interior. The deformation source is a
 398 single prolate ellipsoidal cavity based on previous modelling results¹⁸, located beneath the active vent
 399 and centred at a depth of 12 km below sea level with a semi-major axis of 6000 m and semi-minor
 400 axes of 2000 m¹⁸ (all model variables shown in Supplementary Table 1). The model geometry is
 401 meshed using ~690,000 tetrahedral elements, with greatest mesh density around the deformation
 402 source, on the surface of the model, and at the cGPS site locations. More recent deformation
 403 modelling results for SHV⁴⁵ provide an alternative source geometry to that used in our study¹⁸,
 404 however if we had used the updated source geometry it would not have altered the modelled temporal
 405 deformation or our conclusions; a comparative figure is shown in Supplementary Figure 7.

406

407 Two different boundary conditions are applied independently to the surface of the deformation source
 408 to compare their results in parallel; a boundary load overpressure (ΔP) or a volumetric expansion
 409 normal to the surface of the source (ΔV). We use both ΔP and ΔV to capture the full range of
 410 viscoelastic behaviours in response to a stress-based or strain-based boundary condition³⁰,
 411 respectively, and to further enable applicability of our broader results to forward (often ΔP) and
 412 inverse (often ΔV) volcano geodetic modelling schemes. We assume ‘pure’ ΔP and ΔV endmembers
 413 to focus on first-order differences, whereas there is likely mixed-mode deformation and dynamical
 414 relationships between the two⁵¹.

415

416 The model mechanical properties are informed by a 3D seismic P-wave (V_P) tomography model³⁸. V_P
 417 values are converted to a dynamic Young’s Modulus (E_D) and density (ρ) using⁵²:

$$\rho = 1.6612v_p - 0.4721v_p^2 + 0.0671v_p^3 - 0.0043v_p^4 + 0.000106v_p^5 \quad (1)$$

$$E_D = \frac{v_p^2 \rho (1 + \nu)(1 - 2\nu)}{1 - \nu} \quad (2)$$

418 where ν is the Poisson's Ratio of 0.25. We convert from a dynamic Young's Modulus (E_D) to a static
 419 Young's Modulus (E) using a conservative scaling factor of 2 ($E = E_D/2$), as a static Young's Modulus
 420 is more appropriate for volcanic deformation timescales⁵³, and E_D is commonly 2-13 times larger than
 421 E ⁵⁴. The resulting range of E is between ~ 1 and ~ 100 GPa (Figure 2) and appropriate for volcanic
 422 regions⁵³.

423

424 The model has a temperature-dependent viscoelastic rheology using a Standard Linear Solid (SLS)
 425 viscoelastic representation. A viscoelastic rheology is chosen to better represent the crust beneath
 426 SHV where increased ductility relating to thermal perturbations caused by the long-lived magmatic
 427 system likely invalidates the use of an elastic rheology^{12,18,30,55–57}. In our temperature-dependent
 428 viscoelastic setup⁵⁰, we first solve for a steady-state temperature distribution assuming a surface
 429 temperature of 293 K, a magma temperature of 1123 K⁵⁸, and an initial geothermal gradient of 30
 430 K/km¹⁸. The resultant temperature distribution is shown in Figure 2, and has a geothermal gradient of
 431 54 K/km above the deformation source, and 28 K/km beneath. The temperature (T) is used to
 432 calculate the value of viscosity (η) used in the viscoelastic deformation model via an Arrhenius
 433 formulation:

$$\eta = A_D \exp\left(\frac{H}{RT}\right) \quad (3)$$

434 where A_D is the Dorn Parameter (10^9 Pa s)^{12,55,59}, H is the activation energy (120 kJ/mol)^{18,60} and R is
 435 the universal gas constant. The distribution of the Shear Modulus between the two branches of the
 436 SLS model is a poorly constrained parameter for volcanic materials and crustal rocks. We therefore
 437 take the simplest approach and split the Shear Modulus equally across the two branches of the SLS
 438 model ($\mu_1 = \mu_0 = 0.5$), which also maintains consistency with previous studies at SHV^{18,45} and other
 439 volcanoes^{12,30,50,51,59,61–63}. The resultant viscosity distribution is shown in Figure 2, with elevated
 440 viscosities at the cold model surface, and reduced viscosities around the hot deformation source.

441

442 A SLS viscoelastic representation is chosen over a Maxwell representation because the SLS model is
 443 the simplest viscoelastic representation to demonstrate time-dependent asymptotic creep and
 444 asymptotic stress relaxation, and to fully recover strain over a sufficient timescale^{30,64,65}. In contrast, a

445 Maxwell viscoelastic representation describes a fluid behaviour that produces infinite, linear creep,
446 and has no time-dependent strain recovery^{64,65}, and is therefore considered unsuitable for modelling
447 volcanic deformation³⁰. We show a comparison of SLS and Maxwell viscoelastic representations to
448 highlight these effects (Supplementary Figure 8). The results demonstrate how a constant 10 MPa
449 pressure in a Maxwell model produces increasing deformation with time, due to limitless viscoelastic
450 creep, culminating in over 9 m of vertical deformation after 10 years. Horizontal deformations in the
451 Maxwell model also show rapid short-term oscillations in velocity, producing patterns never recorded
452 (to our knowledge) in geodetic datasets.

453

454 *Modelling Approach*

455 We model the recorded temporal deformation patterns at SHV by testing a range of time-dependent
456 boundary conditions (source functions) applied to the deformation source in a series of forward
457 models (Figure 3). Our temporal source functions mimic possible first-order stress states in a
458 magmatic system: constant with time (static), linearly increasing with time (ramp), instant pulse
459 (rectangle), and gradual pulse (trapezium). The pulse is 6 years in duration to reflect a possible period
460 of elevated magma supply; shorter pulse durations were also tested and showed similar results.
461 Source functions are defined between 0 and 1, and used as a time-dependent scaling factor that is
462 multiplied with the defined overpressure (ΔP) or volume change (ΔV). A value of 10 MPa for ΔP is
463 used throughout the study; in the ramp source function this translates into a rate of 1 MPa/yr. In the
464 ΔV models a prescribed displacement of 0.39 m is uniformly applied normal to the boundary surfaces
465 of the source to generate a volume change. The value of 0.39 m was derived from the average
466 source boundary displacement in an equivalent elastic model with a ΔP of 10 MPa. Our first-order
467 approach produces broadly equivalent amounts of (elastic) reservoir deformation in the ΔP and ΔV
468 viscoelastic models. As the focus of our study is to reproduce and interpret the temporal deformation
469 patterns, rather than the absolute spatial magnitudes of deformation, we do not vary the values of
470 overpressure or volume change to produce a best-fit between absolute recorded and predicted
471 deformation magnitudes for the time-period in question. All model source functions are compared for
472 a ΔP and ΔV boundary condition; normalised comparisons remove the effect of the absolute value of
473 ΔP and ΔV .

474

475 **Additional References**

476

477 49. Herring, T. A., King, R. & McClusky, S. *Introduction to GAMIT/GLOBK, release 10.4.* (2010).478 50. Hickey, J. & Gottsmann, J. Benchmarking and developing numerical Finite Element models of
479 volcanic deformation. *J. Volcanol. Geotherm. Res.* **280**, 126–130 (2014).480 51. Gregg, P. M., de Silva, S. L. & Grosfils, E. B. Thermomechanics of shallow magma chamber
481 pressurization: Implications for the assessment of ground deformation data at active482 volcanoes. *Earth Planet. Sci. Lett.* **384**, 100–108 (2013).483 52. Brocher, T. M. Empirical relations between elastic wavespeeds and density in the Earth's
484 crust. *Bull. Seismol. Soc. Am.* **95**, 2081–2092 (2005).485 53. Gudmundsson, A. *Rock Fractures in Geological Processes.* (Cambridge University Press,
486 2011). doi:<https://doi.org/10.1017/CBO9780511975684>487 54. Cheng, C. H. Dynamic and static moduli. *Geophys. Res. Lett.* **8**, 39–42 (1981).488 55. Del Negro, C., Currenti, G. & Scandura, D. Temperature-dependent viscoelastic modeling of
489 ground deformation: Application to Etna volcano during the 1993-1997 inflation period. *Phys.*
490 *Earth Planet. Inter.* **172**, 299–309 (2009).491 56. Ranalli, G. *Rheology of the Earth.* (Springer Netherlands, 1995).492 57. Zellmer, G. F. *et al.* Geochemical Evolution of the Soufrière Hills Volcano, Montserrat, Lesser
493 Antilles Volcanic Arc. *J. Petrol.* **44**, 1349–1374 (2003).494 58. Murphy, M. D., Sparks, R. S. J., Barclay, J., Carroll, M. R. & Brewer, T. S. Remobilization of
495 andesite magma by intrusion of mafic magma at the Soufriere Hills volcano, Montserrat, West
496 Indies. *J. Petrol.* **41**, 21–42 (2000).497 59. Gregg, P. M., De Silva, S. L., Grosfils, E. B. & Parmigiani, J. P. Catastrophic caldera-forming
498 eruptions: Thermomechanics and implications for eruption triggering and maximum caldera
499 dimensions on Earth. *J. Volcanol. Geotherm. Res.* **241–242**, 1–12 (2012).500 60. Murase, T. Viscosity and Related Properties of Volcanic Rocks at 800°C to 1400°C. *J. Fac. Sci.*
501 *Hokkaido Univ.* **1**, 487–584 (1963).502 61. Hickey, J. *et al.* The Ups and Downs of Volcanic Unrest: Insights from Integrated Geodesy and
503 Numerical Modelling. in *Advances in Volcanology* (Springer, 2017).

504 62. Zhan, Y., Gregg, P. M., Le Mével, H., Miller, C. A. & Cardona, C. Integrating Reservoir

- 505 Dynamics, Crustal Stress, and Geophysical Observations of the Laguna del Maule Magmatic
506 System by FEM Models and Data Assimilation. *J. Geophys. Res. Solid Earth* **124**, 13547–
507 13562 (2019).
- 508 63. Zhan, Y. & Gregg, P. M. How Accurately Can We Model Magma Reservoir Failure With
509 Uncertainties in Host Rock Rheology? *J. Geophys. Res. Solid Earth* **124**, 8030–8042 (2019).
- 510 64. Christensen, R. *Theory of Viscoelasticity: An Introduction*. (Dover Publications, 1982).
- 511 65. Crawford, R. J. *Plastics Engineering*. (Butterworth-Heinemann, 1998).
- 512

513

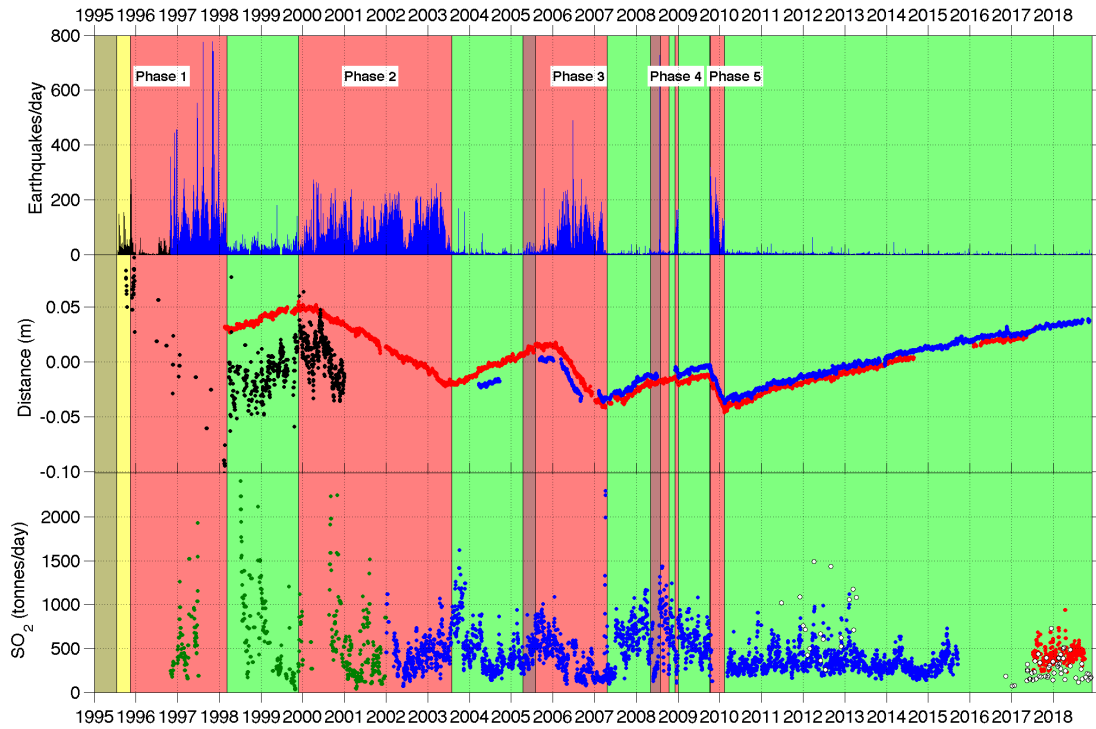
SUPPLEMENTARY MATERIAL:

514

515 **Supplementary Figure 1**

516

517



518

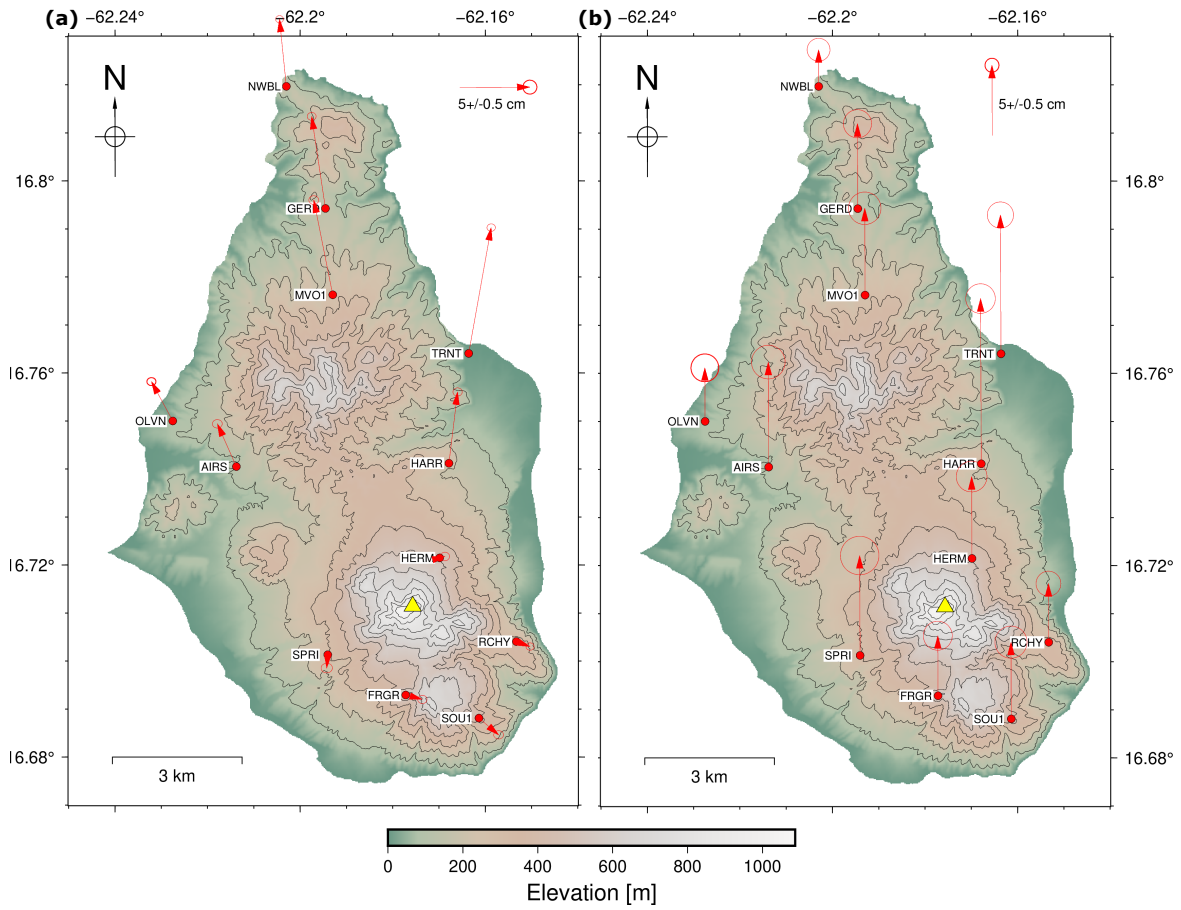
519 **Supplementary Figure 1:** Summary of seismic, deformation and SO₂ flux data for the current
 520 eruptive episode of SHV. Top: Number of seismic events detected and identified by the seismic
 521 system. Middle: Radial displacement of cGPS stations MVO1 (red) and NWBL (blue) smoothed with a
 522 7-day running mean filter, plus the GPS height of HARR (black). Bottom: Measured daily SO₂ flux,
 523 filtered with a 7-day running median filter, showing COSPEC (green), old DOAS (blue), new DOAS
 524 (red), and traverse (white) data.

525

526 **Supplementary Figure 2**

527

528



529

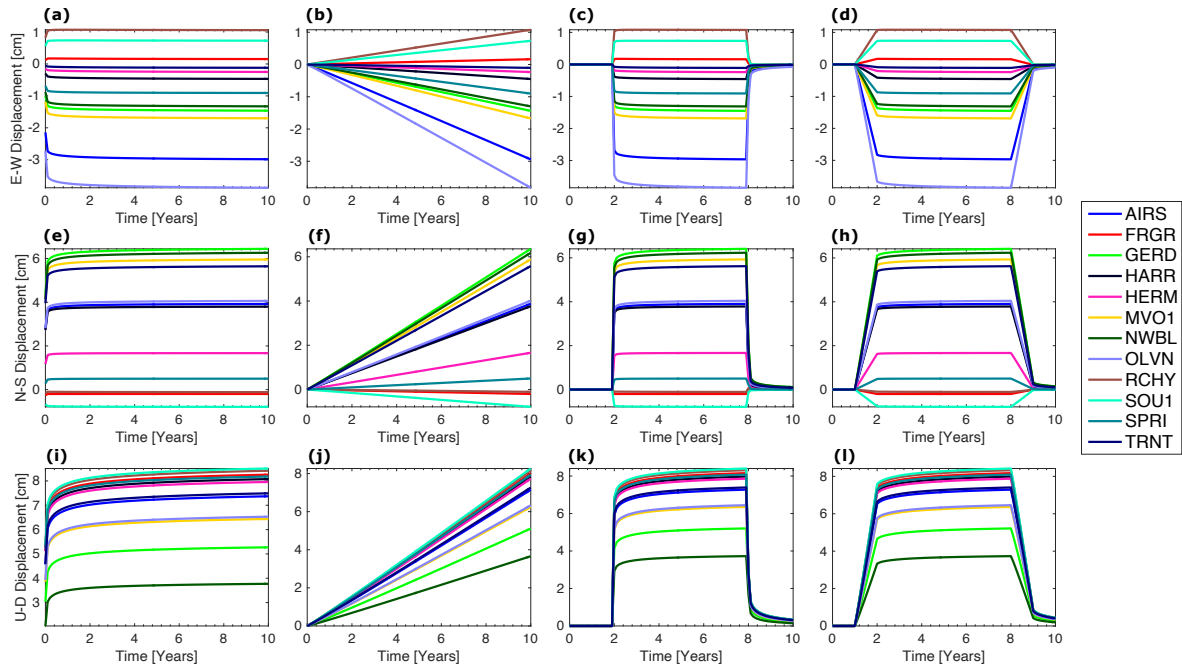
530 **Supplementary Figure 2:** *Spatial deformation recorded by cGPS between 25/01/2010 and*
 531 *22/09/2018. (a) Horizontal deformation. (b) Vertical deformation. Ellipses show 95% confidence*
 532 *bounds. Yellow triangle indicates the location of the SHV vent.*

533

534 **Supplementary Figure 3**

535

536



537

538 **Supplementary Figure 3:** Model results for the four source functions using a ΔP boundary condition,

539 shown for all cGPS sites. (a-d) Predicted modelled east-west displacements. (e-h) Predicted modelled

540 north-south displacements. (i-l) Predicted modelled vertical displacements. The four source functions

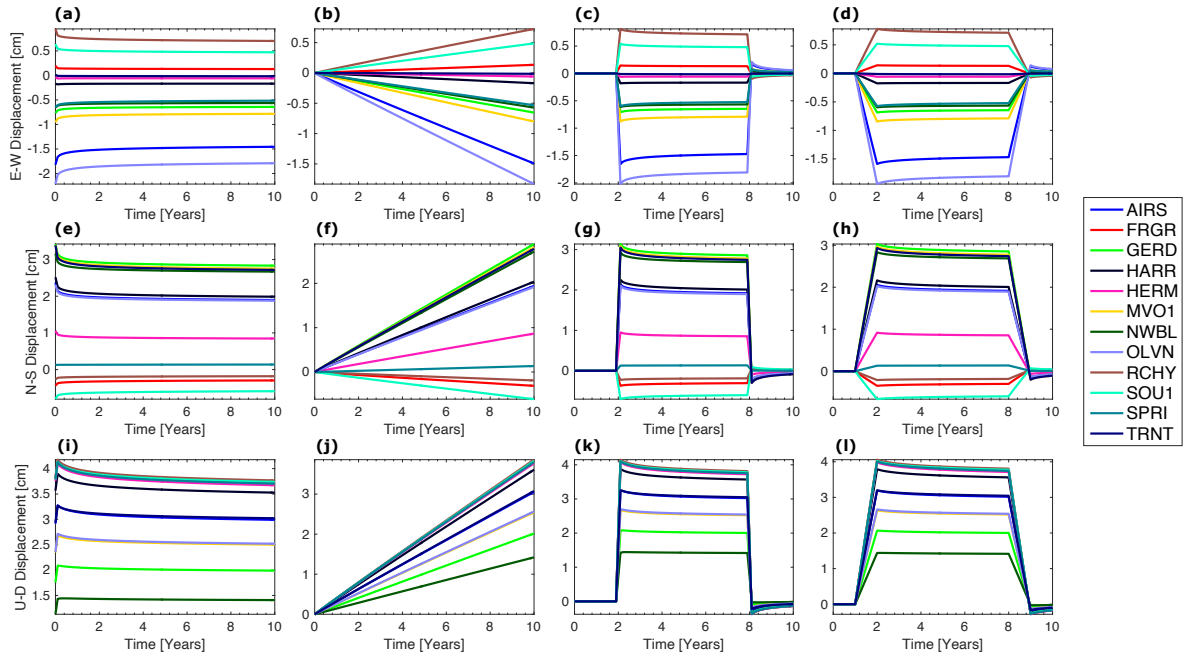
541 are static (a, e, i), ramp (b, f, j), instant pulse (c, g, k), and gradual pulse (d, h, l), as seen in Figure 3.

542

543 **Supplementary Figure 4**

544

545



546

547 **Supplementary Figure 4:** Model results for the four source functions using a ΔV boundary condition,

548 shown for all cGPS sites. (a-d) Predicted modelled east-west displacements. (e-h) Predicted modelled

549 north-south displacements. (i-l) Predicted modelled vertical displacements. The four source functions

550 are static (a, e, i), ramp (b, f, j), instant pulse (c, g, k), and gradual pulse (d, h, l), as seen in Figure 3.

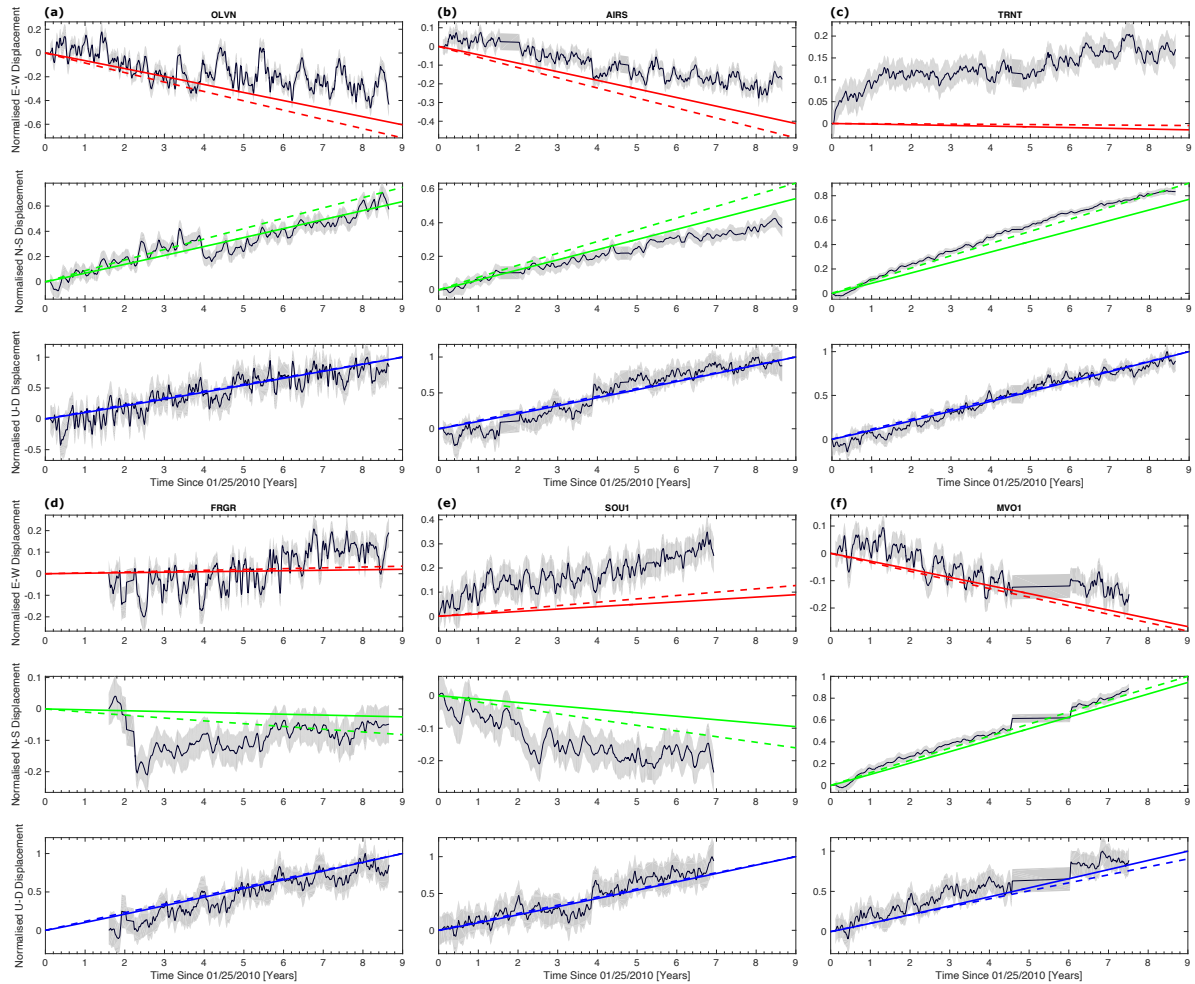
551

552

553 **Supplementary Figure 5**

554

555



556

557 **Supplementary Figure 5: Normalised model-data comparison for different cGPS sites and the ramp**

558 *temporal source function. The cGPS sites are (a) OLVN, (b) AIRS, (c) TRNT, (d) FRGR, (e) SOU1,*

559 *and (f) MVO1. Normalised surface displacements are shown for the east-west (red), north-south*

560 *(green) and vertical (blue) components, where the thin black line and shaded grey region display the*

561 *recorded deformation and error bounds, and the solid and dashed coloured lines show the model*

562 *results for a ΔP and ΔV boundary condition, respectively. Model and data are normalized to the*

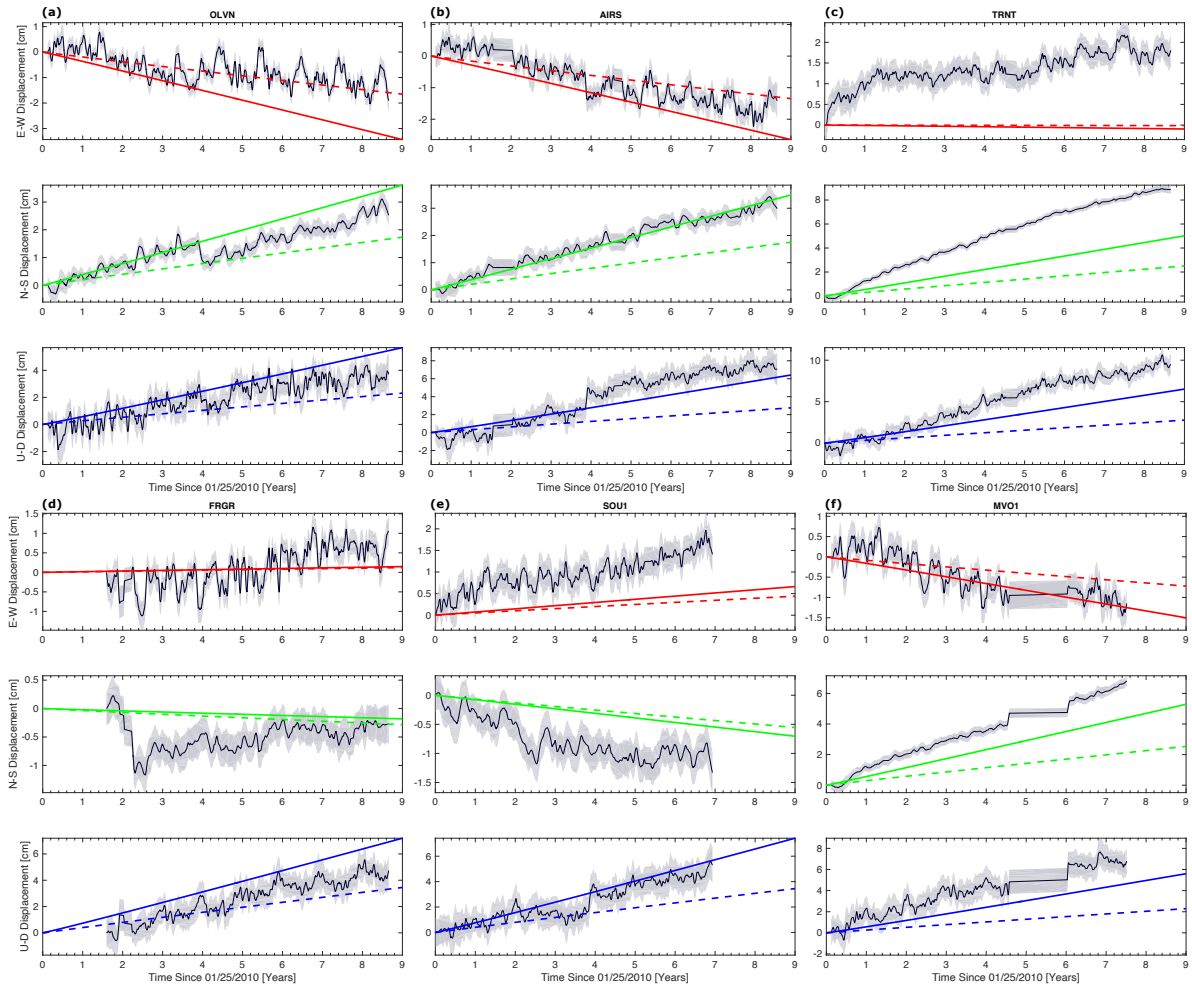
563 *maximum absolute deformation across the 3 components (in this case vertical).*

564

565 **Supplementary Figure 6**

566

567



568

569 **Supplementary Figure 6:** Absolute model-data comparison for different cGPS sites and the ramp

570 temporal source function. The cGPS sites are (a) OLVN, (b) AIRS, (c) TRNT, (d) FRGR, (e) SOU1,

571 and (f) MVO1. Absolute surface displacements are shown for the east-west (red), north-south (green)

572 and vertical (blue) components, where the thin black line and shaded grey region display the recorded

573 deformation and error bounds, and the solid and dashed coloured lines show the model results for a

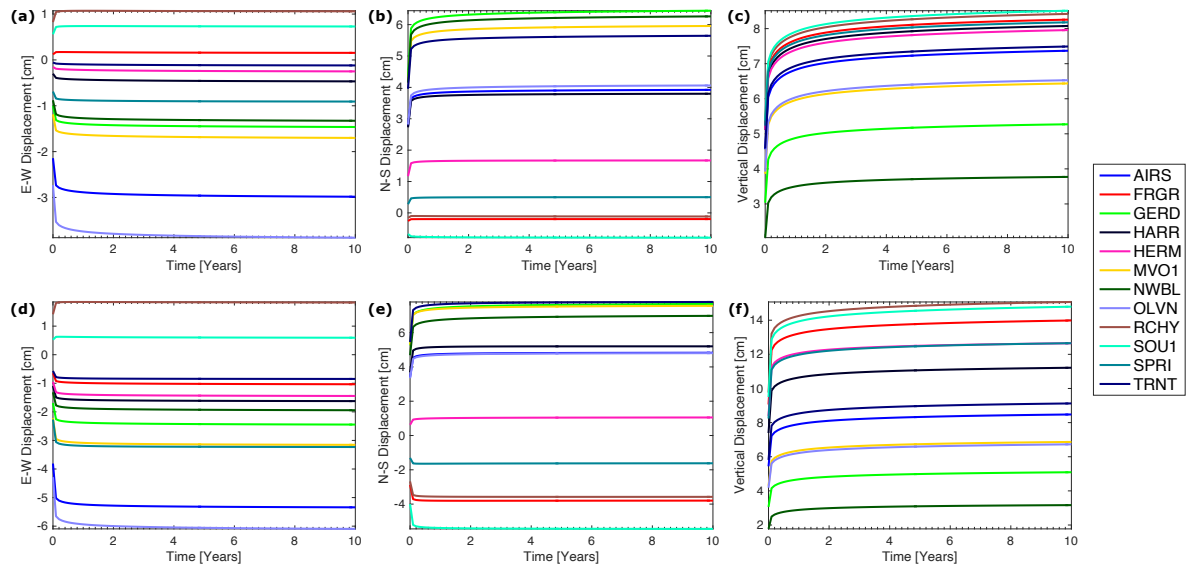
574 ΔP and ΔV boundary condition, respectively.

575

576 **Supplementary Figure 7**

577

578



579

580 **Supplementary Figure 7:** Comparison of modelled temporal deformation for the source geometry

581 employed in our study and the source geometry from Gottsmann et. al., 2020 [35], using a static

582 source pressure. (a-c) Modelled east-west (a), north-south (b) and vertical (c) deformation

583 components for 12 cGPS sites using source parameters shown in Supplementary Table 1. (d-f)

584 Modelled east-west (d), north-south (e) and vertical (f) deformation components for 12 cGPS sites

585 using source parameters from Gottsmann et. al., 2020 [45]. Despite slight differences in the spatial

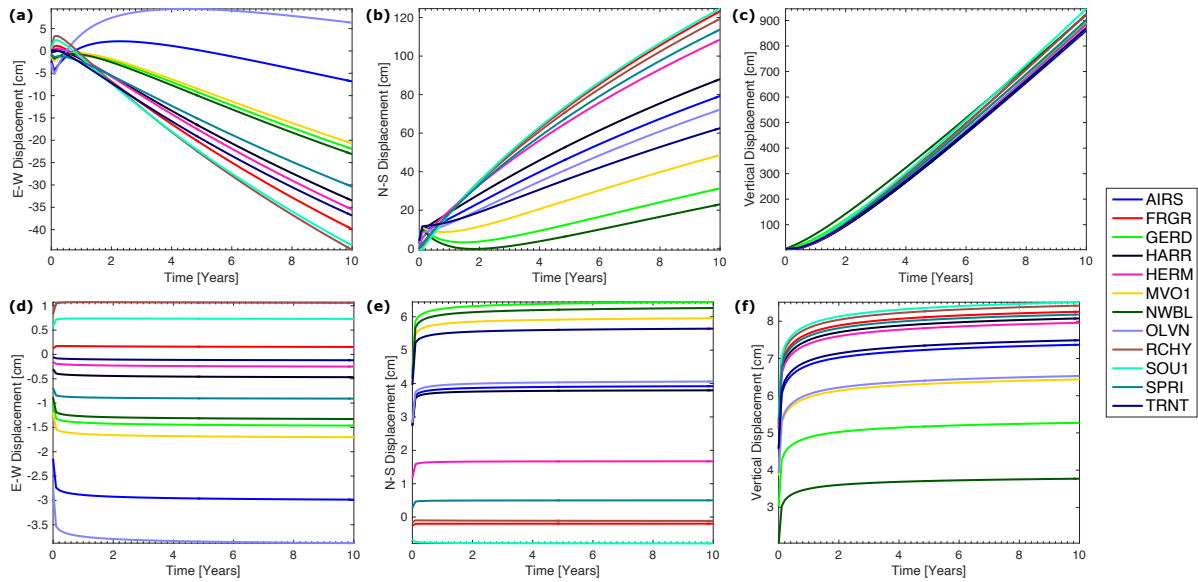
586 magnitudes of some results, the temporal trends across all results are identical.

587

588 **Supplementary Figure 8**

589

590



591

592 **Supplementary Figure 8:** Comparison of Maxwell and SLS viscoelastic representations, for a

593 constant source pressure. (a-c) Modelled east-west (a), north-south (b) and vertical (c) deformation

594 components for 12 cGPS sites using a Maxwell viscoelastic. (d-f) Modelled east-west (d), north-south

595 (e) and vertical (f) deformation components for 12 cGPS sites using a SLS viscoelastic

596 representation. Note the change in scale between Maxwell (a-c) and SLS (d-f), as well as the

597 difference in temporal evolution of the deformation.

598

599

600 **Supplementary Table 1**

601

Parameter	Definition	Value	Unit
X	Source Longitude	-62.1757	°
Y	Source Latitude	16.7114	°
Z	Source Depth	12,000	m
ΔP	Source Pressure	10	MPa
ΔV	Source Volume Change	0.39	m
a	Semi-major Axis	6000	m
b	Semi-minor Axes	2000	m
V_P	P-wave Velocity	1.4 – 8.7	km/s
E_D	Dynamic Young's Modulus	Eq. 2	GPa
ρ	Density	Eq. 1	kg/m ³
ν	Poisson's Ratio	0.25	-
E	Static Young's Modulus	$E_D/2$	GPa
T_{surf}	Surface Temperature	293	K
T_{mag}	Magma Temperature	1123	K
dT/dZ	Geothermal Gradient	30	K/km
η	Viscosity	Eq. 3	Pa s
A_D	Dorn Parameter	10^9	Pa s
H	Activation Energy	120	kJ/mol
R	Universal Gas Constant	8.314	J/(mol K)
k	Thermal Conductivity	3	W/(m K)
C_p	Heat Capacity	1000	J/(kg K)
μ_0, μ_1	Fractional Modulus	0.5	-

602

603

604